COMMON DEFECTS IN POWDER BED FUSION TECHNOLOGIES

Abstract

This document aims to propose a classification for common defects found in materials processed by powder bed fusion technologies. Indeed, by studying the state of the art, it appears there is no synthetic document which proposes a classification of all defects found in parts made with this process. Thus, a classification is hereafter proposed, widely inspired by a work done in the framework of casting of aluminum alloys by Bonollo and Fiorese. The document tries to highlight the physical origin of each defect by explaining it with the elements found in the literature. For each defect, it is specified if there is a particularity due to the process (EBM or LBM) or the alloy (AS7G06, Ti6-4 or 718) employed.

DATE: 04/11/2019

REFERENCE: LIV-M-L10-508-V1

Author(s	*Fonction(s) & name(s)*	*Reseach Engineer*	*Benoit TRANCHAND*
Checker(s)	*Fonction(s) & name(s)*	*Project Leader* *Quality Manager*	*P.O. Jonathan HUGUES* *Stéphane BENAZET*
Approver	*Fonction & name*	*Head of Metallic Materials Department*	*Simon PERUSIN*

Table of Contents

Revision Table

Issue	Date	modified §	Evolution summary	Modified by
0	04/11/2019		Creation	All

Table of illustrations

Table of abbreviation

AM	:	Additive Manufacturing
EBM	:	Electron Beam Melting
EDX or EDS	:	Energy-Dispersive X-ray Spectrometry
LBM	:	Laser Beam Melting
LOF	:	Lack Of Fusion
NDT	:	Non Destructive Test
PREP	:	Plasma Rotating Electrode Process
X-ray CT	:	X-ray Computed Tomography

1 Introduction

Additive manufacturing by powder bed fusion generates an important number of defects. All these defects are highly diverse in terms of their nature their origin, size and shape. According to literature review, there are few studies which propose exhaustive defects description. The information, for a couple of processes such as EBM or LBM and alloy used, has to be compiled. Thus, to our knowledge, no defects database exist for powder bed fusion processes. This type of database has the benefit to list all the defects that can be found in these processes and to classify them as a function of their characteristics such as morphology or origin. In the following literature review, the classification by the origin of the defects has been chosen.

This classification will allow the organization of a defect database in the framework of the ANDDURO project. This database will be supplied by defect found in the analysis made in the framework of the project such as microscopic analysis or XRays CT scans.

2 Semantic precision and need of a database

2.1 Semantic precision

The term “defects” will be used in the following document by simplification. The reader has to keep in mind this document will not introduce acceptance criteria for additive manufacturing. Indeed, in most processes, the word “defect” is linked with a quality characteristic of the material. If defects are detected, at least, an additional justification is needed to use the part, in the worst case, the part has to be scrapped, and in an intermediate case, the part has to be repaired.

An object named “defect” hereafter will refer to an undesired heterogeneity in the material which may be detrimental [1] for the mechanical behavior of the fabricated material such as void, pore, crack, detrimental phases, inclusions, heterogeneity of microstructure …

2.2 Need of a database

To the best of our knowledge, there is no paper dealing with a quasi-exhaustive defects database for additive manufacturing. According to this literature review, there was no pertinent result neither on the scientifics editors website nor on common research engine with the following keywords: “defects database EBM”, “defects database LBM”, “defect database additive manufacturing”, “defect classification additive manufacturing”, “defect classification EBM” or “defect classification LBM”.

In most cases, the authors of papers on defects in metallic additive manufacturing only deal with a specific type of defect, from its origin to the solution to mitigate it.

Moreover, by comparing with more traditional processes as casting or forging, papers found dealing with the development of a defects database are not widespread. The most relevant study found is proposed by the team lead by Bonollo et Fiorese [2], [3]. The following defects classification dealing with powder bed fusion proposed is widely inspired by this work as developed in the following paragraph.

3 Method of classification

The method proposed by the IRT Saint Exupéry used hereafter (Table 1 and Table 2) to classify defects and imperfections in powder bed fusion technologies is widely derived from the work of Bonollo et al. [2], [3] in the framework of the StaCast project, focusing on the development of new quality and design standards for aluminium alloys cast products. They would like to make more understandable the physical origin of the defects and imperfections produced during casting processes than the existing classifications [4]–[6].

The principle of this classification is illustrated in the Figure 1. Authors chose to classify defects among three levels:

1- The first level refers to the location of the defect: internal, external or geometrical. For this level, it could be noted that a subsurface defect, internal, could have consequences on the surface of the studied part. So such defect could induce surface, external, or geometrical defect. The first level will be noted with the letters A, B or C.
2- The second level refers to the physical origin of the defect. The physical origins are gases, lack of fusion (often abbreviated with “LOF”), undesired phases, balling… The second level will be noted with a number next to the letter of the first level: A1 or B3 for examples.

3- The third level specifies the second level when necessary. It allows to strongly link the formation of the defect with a process parameter.

1st Level	2nd Level		3rd Level	
A Internal Defects and Imperfections	A1	Shrinkage defects and imperfections	A1.1	Macro-shrinkage
			A1.2	Interdendritic shrinkage
			A1.3	Layer porosity
	A2	Gas-related defects and imperfections	A2.1	Air entrapment porosity
			A2.2	Hydrogen porosity
			A2.3	Vapor entrapment porosity
			A2.4	Lubricant and/or die release agent entrapment porosity
	A3	Filling-related defects and imperfections	A3.1	Cold joint
			A3.2	Lamination
			A3.3	Cold shot
	A4	Undesired phases	A4.1	Inclusion
			A4.2	Undesired structure
	A5	Thermal contraction defects and imperfections	A5.1	Cold crack
			A5.2	Hot tear, hot crack

Figure 1: Extract of the classification proposed by Fiorese et al. [3] : case of internal casting defects and imperfection.

Several issues encountered for proposing this classification and then for describing each phenomenon have to be highlighted.

The main issue to be resolved for classifying is the identification of the physical phenomenon. As said previously, lot of studies allow the definition of a process map and identify key parameters which, if they are outside this process map, cause an increase of defect rate in the material. In most studies, the physical phenomenon linked to defects creation is not identified.

In the same way, a process can lead to the creation of another type of defect. For example, balling [7]–[9] is a surface defect as it will be described in more details in the following paragraphs (§4.2). If this type of defect is recoated by a new layer of powder, it leads to an irregularity of the powder bed and may lead to a lack of fusion. Thus, the physical origin of the lack of fusion is an irregularity of the powder bed and not the balling phenomenon.

Finally, in the framework of the ANDURRO project, two different processes, EBM and LBM, are used in combination with three alloys (AS7G06, Ti6-4 and Ni718). Sometimes, a couple of {process and alloy} presents affinity or not to produce a type of defect. These specificities are mentioned at the end of the description of the formation of the defects.

Our proposition of classification is presented in the Table 1 and the Table 2. If the content of the Table 1 may be considered as exhaustive, not all surface defects are listed in the Table 2: only surface defects which induce bulk defects after being recovered by the following layer are developed. The content of the Table 2 may be completed later if necessary. For a more exhaustive classification, Airbus [10] wrote a technical specification for additive manufactured parts in alloy Ti6-4.

The description of each class is then developed in the §4.1 for the Table 1 and in the §4.2 for the Table 2.

1st Level	2nd Level		3rd Level	
A Internal defects	A1	Gas-related defects	A1.1	Powder Induced pores
			A1.2	Vaporized alloys element
			A1.3	Inert gas entrapment
			A1.4	Hydrogen pores
	A2	Shrinkage defects	A2.1	Shrinkage defect
	A3	Lack of fusion defects	A3.1	Hatching induced LOF
			A3.2	Interlayer LOF
	A4	Cracks	A4.1	Liquation cracking
			A4.2	Solidification cracking
			A4.3	Strain-age cracking (SAC)[1]
			A4.4	Ductility Dipe Cracking (DDC)[1]
	A5	Undesired phases	A5.1	Inclusion
			A5.2	Precipitates
			A5.3	Oxydes
			A5.4	Microstructural heterogeneity

Table 1: Classification of internal defects.

1st Level	2nd Level		3rd Level	
Surface defects	B1	Melt pool induced	B1.1	Balling
			B1.2	Spattering
			B1.3	Swelling
	B2	Cracks	B2.1	Residual stress induced

Table 2: Classification of surface defects.

[1] Strain-Age Cracking and Ductility Dipe Cracking are currently found in Ni based alloys with a bad weldability such as IN738 or U230. It is mentionned here for memory and will not be developped later on.

4 Classification of defects

4.1 Internal defects

4.1.1 Gas related defects

Internal defect		
A	Internal defect	I
A1	Gas-related defect	II
A1.1	Powder induced pores	III

Definition:

The powder induced porosity consists of spherical cavities due to gas entrapped (in most of the case, Argon, due to the powder sources used) in the powder during its production (Figure 2). When the powder is melt by the electron or the laser beam, depending on the viscosity, the distance of the gas bubble to the free surface and the cooling rate, the gas bubble can remain trapped in the melt pool and then in the solidified material.

Sames et al. [11] point out that gas related porosity in EBM parts is an illustration of physical phenomena during the process: the high cooling rate combined to the low pressure gradient between the gas bubble in the melt pool and the chamber deteriorates the degassing conditions. Thus, the outgassing of the melt pool is usually difficult. Despite a lowest pressure gradient in case of LBM, no article mentions this effect in the literature.

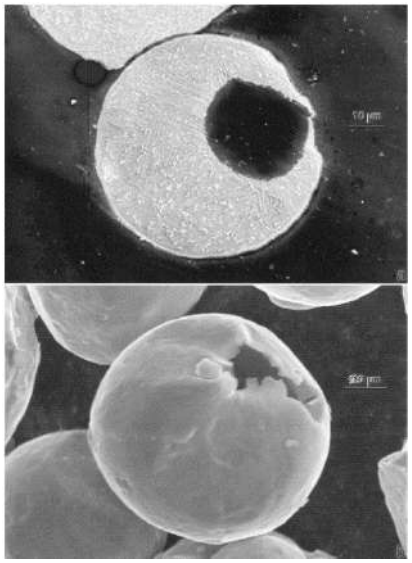

Figure 2: Gas voids in Ti6-4 powder : Optical metallography of a powder particle containing pore (up) - SEM view of a gas bubble (down) (from [17]).

Morphology

The morphology of gas related defect is supposed to be rather spherical. With this assumption, for alloy Ti6-4, Cunningham et al. [12] assume the average equivalent diameter of powder induced pores is beside 10 µm with a maximum size around 40 µm. This average size seems to be correlated with the average equivalent diameter of voids found in the powder: they do not assess that a potential re-growth of the voids during the melting of the upper layers occurs. As mentioned in a further paragraph (§A1.4 – hydrogen porosity), this phenomenon has already been identified, in particular for AlSi10Mg alloy [13].

Tammas-Williams [14] showed the regrowth of gas pores after heat treatment in EBMed alloy Ti6-4. But they attribute the gas porosity exclusively to inert gas initially entrapped in the powder.

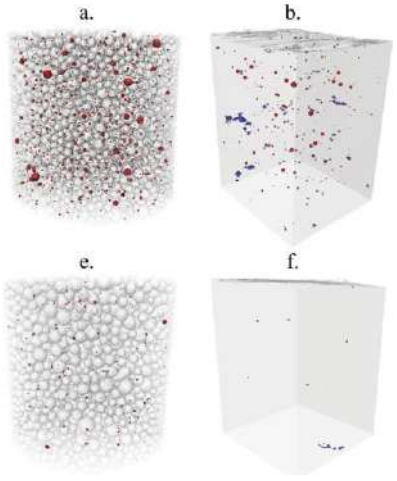

Figure 3: X-ray CT scans comparing two types of Ti6-4 powder obtain by GA (a) and PREP (e) then the resulting material as-built by EBM (b) and (f) (from [12]).

Physical origin

As mentioned previously, the method of powder production is a key parameter of the gas induced porosity. The literature show that powder produce by Plasma Rotating Electrode Process (PREP) contain less gas pores inside the powder particles than powder produce by Gas Atomisation (GA) or Rotary Atomization (RA) [11], [12], [15], [16] . The gas entrapped is considered to be the gas used during the atomization, i-e in most of the cases Argon for the alloys studied in this document. The use of PREP powder show a clear decrease of the defect density in the raw material as illustrated by Figure 3.

Special features for EBM, LBM, Al, Ti or Ni alloy There is no studies found about gas entrapment neither for LBM process nor for alloy AS7G06.		
A	Internal defect	I
A1	Gas-related defect	II
A1.2	Vaporized element in the melt pool	III

Definition:

The porosity is induced by the vaporization of elements constituting the alloys under the effect of the laser or electron beam.

Morphology

By studying LBMed alloy AS7G06, Rao et al. [13] described the keyhole voids as irregular pores with range between $100\ \mu m$ and few hundreds of microns, often located at melt pool boundaries.

Gong et al. (Gong, Gu, et al. 2014) isolated keyhole voids of LBMed alloy Ti6-4 on micrograph as illustrated in Figure 4. Here, one melt pool with a keyhole geometry is isolated from the bulk material. A void with an irregular shape is clearly visible at the bottom of the melt pool.

Stef [18] specified that defects isolated in Kasperovitch study [19], shown in Figure 5 are keyhole induced defects.

Stef [18] built specimens in process conditions favorable to keyhole mode and then analyzed defects population with a CT scan: he estimated a mean diameter of keyhole induced defect between $25\ \mu m$ and $35 \mu m$ and an aspect ratio between 1.3 and 1.4. Ti6-4

The keyhole induced porosity could be formed at a significant depth. Martin et al. [20] showed pore formation from $100\ \mu m$ depth to $1000\ \mu m$ depth for LBMed alloy Ti6-4 for laser powers ranging from $50W$ to $300W$.

Each alloy, due to its properties, lead to a specific geometry of keyhole defect as shown by Huang et al. [21].

Physical origin

The keyhole mode is well known in the process of electron or laser welding [22] , in particular for welds requiring deep-penetration for which the energy density is higher than for additive manufacturing.

Two regimes of a melt pool are known: the conductive mode and the keyhole mode [23]–[26]. In a conductive regime, the melt pool is only composed only by a liquid phase of the melt alloy whereas in a keyhole regime, the melt pool is composed both by a liquid and a vaporized phase. Under specifics conditions, the material in the keyhole can even form a plasma [27].

The keyhole mode induces multiples phenomenon [22] :

- Large temperature gradient;
- Strong vapor flux;
- Enhancement of the laser absorption;
- Flow directions in the melt pool…

Which are themselves influenced by others such as the presence of oxides on the melt pool surfaces [28]. Stef [18] noted that keyhole mode induces sometimes powder ejection around the laser path.

These phenomenon are intense and interact, thus, it is challenging to obtain a stable keyhole mode.

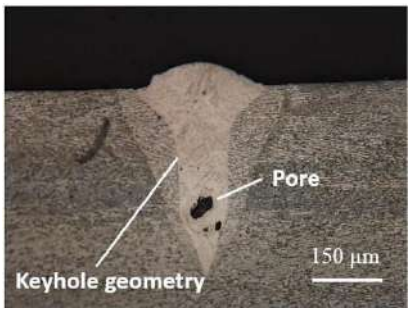

Figure 4: Micrograph of LBMed alloy Ti6-4 showing a keyhole induced pore in [32]

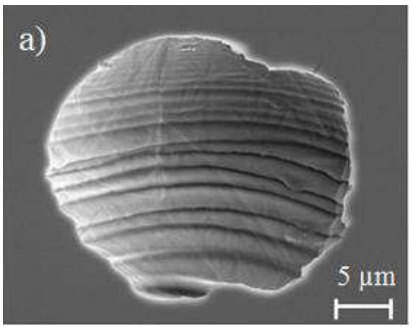

Figure 5 : SEM images of keyhole induced pore in LBMed alloy Ti6-4 [19].

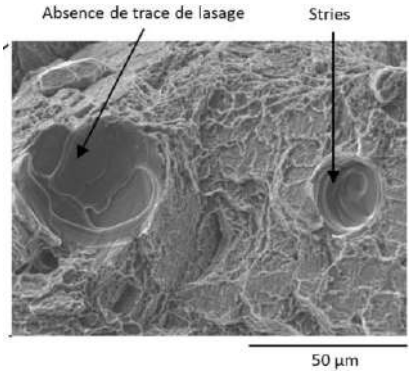

Figure 6 : Fractography showing keyhole induced pores in LBMed alloy Ti6-4 [18]

Zhao and Debroy [29] supported this affirmation by highlighting that between the conductive mode and the keyhole mode, there is an intermediate region where the melt pool mode is unpredictable. As a result, it is tricky to predict the stability of the phenomenon and so to predict the absence of pore. Rai et al. [24] proposed analytical models compared with experimental results for predicting the stability of the keyhole mode laser welding of various metallic alloys.

Nevertheless, some authors succeeded to define processes operating domains. Cunningham et al. [28] proposed a threshold for the formation of a keyhole around $0.5 MW/cm^2$ for LBMed powder Ti6-4. Gong et al. (Gong, Gu, et al. 2014) suggested only a qualitative domain allowing a keyhole mode: low scan speed and high energy density. Martin et al. [20] pointed that turning points of the laser path are favorable areas for keyhole induced pores. They suggested with success to mitigate the laser power near turning points to avoid the keyhole mode.

Special features for EBM, LBM, Al, Ti or Ni alloy

Gong et al. [30] mentioned that the preset parameters of EBM machines is chosen to avoid keyhole. Only parameters chosen by users can lead to a keyhole mode.

Blackburn [31] notes that shielding gas, argon in case of the LBM process, may be found in pore creating by the collapsing of the keyhole.

A	Internal defect	I
A1	Gas-related defect	II
A1.3	Inert gas entrapment	III

Definition:

This type of pores is induced by the entrapment of inert gas of the manufacturing chamber in the melt pool. In specific condition, the melt pool cannot outgas which lead to an entrapment into the raw material.

Morphology

Vilaro [33] assumed this type of voids is spherical and little between 10µm and 50µm of diameter for alloy Ti6-4. Kimura and Nalamoto [34] highlighted voids of few hundred of micrometers in alloy AS7G03, an alloy close to alloy AS7G06, as shown in Figure 7.

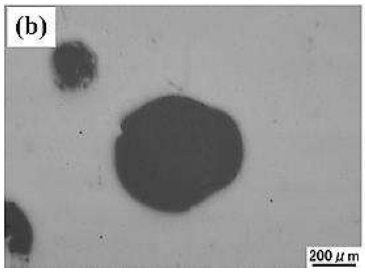

Figure 7: Micrography of AS7G03 specimen LBMed under high energy conditions (from [34]).

Physical origin

There are some consistent explanations in the literature. The inert gas of the chamber is contained into the spaces between the powder particles. As the melt pool is firstly created in surface of the powder bed, it can form a sort of cover on a layer of unmelted powder with gas. Thus, function of the melt pool properties, gas can be entrapped into the melt pool during the solidification. Kimura and Nalamoto [34] measured the gas present in the voids with a Quadrupole Mass Spectrometer (QMS). They found a high rate of Argon (67%) that they attributed only to the gas present in the manufacturing chamber.

With regard to the “powder induced defects” described previously, it is a regrettable fact that they did not analyze the powder, especially since the powder is produced by gas atomization.

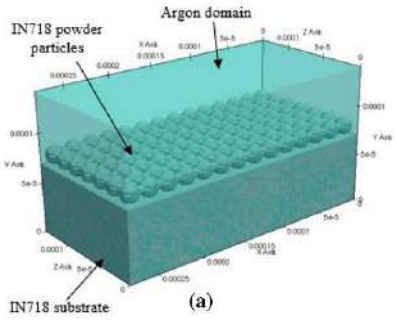

Figure 8: Schema of the simulation model of alloy 718 from [35].

Nevertheless, Aggarwal et Kumar [35], with the support of simulation, questioned the possibility of inert gas entrapment in the case of LBMed alloy 718. They simulated the melt process of a layer of 20 µm of Ni718 powder with a laser of 100 µm of spot diameter, 100 W of power and 700 $mm.s^{-1}$ of velocity. They concluded that significant convective flow of the melt pool allow the rejection of inert gas trapped in the powder bed. It have to be noticed that a strong hypothesis is made by the authors for the simulation about the layer thickness of powder. Usually in LBM process, the layer thickness is around 40 µm with a powder of [20 ; 63 µm] range.

Kimura et Nalamoto [34] suggested some solutions to mitigate this effect as an increasing of the apparent density of the powder bed, decreasing the gas solubility by decreasing the volume of the melt pool (either by decreasing the powder bed thickness or by decreasing the laser power) or reduce the partial pressure of gas into the manufacturing chamber.

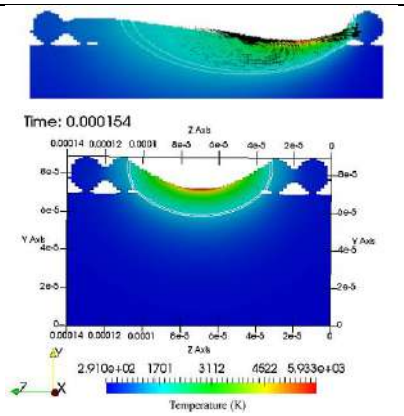

Figure 9: Results of the simulation - Up: Temperature map of the melt pool surrounded by velocity vectors along the XZ plane – Down : Temperature map of the melt pool along the YZ plane from [35].

Special features for EBM, LBM, Al, Ti or Ni alloy

EBM process is not concerned due to the partial vacuum in the manufacturing chamber ($10^{-3}Pa$ of He).

A	Internal defect	I
A1	Gas-related defect	II
A1.4	Hydrogen porosity	III

Definition:

This porosity is induced by entrapment in the melt pool of hydrogen gas coming from moisture of the powder or present in the manufacturing chamber. In specific condition, the melt pool cannot outgas which lead to an entrapment into the raw material. This type of porosity is described and known as “metallurgical pores” in welding process [36], [37].

Morphology

These voids are rather spherical within the melt pool (not at the boundary). Rao [13] exhibits spherical pores located in the melt pool cores, with a diameter below 100 µm (Figure 10) for LBMed alloy A357. Sallica-Leva [38] mentions the presence of hydrogen porosity in LBMed alloy Ti6-4 but does not precise the morphology.

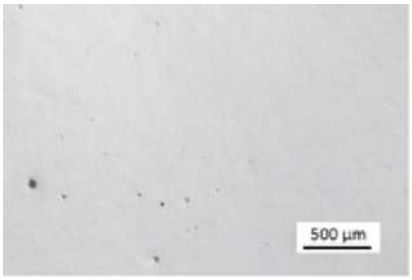

Figure 10 : Hydrogen porosity in LBMed alloy AlSi10Mg modified from [13].

Physical origin

The hydrogen related porosity is due to the local hydrogen content which is higher than the maximum solubility of the molten pool [31], [38], [39].

As shown by Lakomski et Kaliunyuk [40] in Figure 11, despite the solubility of the hydrogen in pure titanium increases with the decreasing of temperature, there is an important decrease at the melting point. Then, due to the decreasing of the solubility, gas bubbles are formed and remain entrapped in the melt pool during the solidification. Most of hydrogen bubbles are produced at the solidification front as illustrated by Figure 12 [39], [41]. Li et al. [42] proposed an analytical model for the nucleation and the growth of hydrogen pores in casted alloy AlSi7Mg0.3.

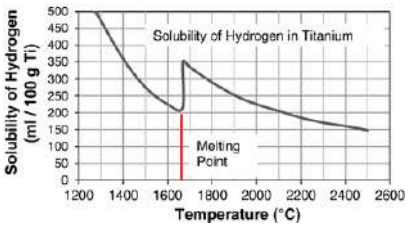

Figure 11 : Solubility of hydrogen in titanium from [40].

The hydrogen mainly comes from the moisture of the powder. Weingarten et al. [39] reminded that moisture reacts with the aluminum to produce aluminum oxide and dihydrogen according to the equation:

$$3H_2O + 2Al \rightarrow Al_2O_3 + 3H_2$$

So, the main parameter to manage to mitigate the hydrogen porosity is hydrogen content in powder.

In case of LBMed alloy AlSi7Mg0.6 (GA powder), Yang [43] estimate that 96% of the gas content is hydrogen whereas Kimura and Nakamoto [34] estimated that 67% were argon and 30% were hydrogen for LBMed alloy AlSi7Mg0.3 (GA powder).

Weingarten et al. [39]noticed that the last scanned layer does not present spherical pores as illustrated by Figure 13. They assumed the previous layers are heat treated, inducing an expansion of the entrapped gas in the matrix which have a lower yielding point at high temperature. They verify their assumption by submitted the specimen to a heat treatment at 550°C: they observe the formation of gas pores of few millimeters of diameter.

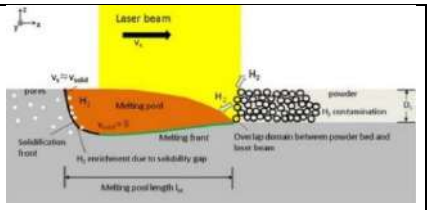

Figure 12: Schema of hydrogen entrapment during LBM process from [39].

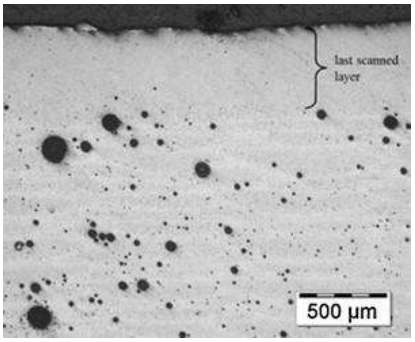

Figure 13: Micrography of the last layers of LBMed alloy AlSi10Mg [39].

<u>Special features for EBM, LBM, Al, Ti or Ni alloy</u>

No hydrogen porosity is explicitly reported for alloy 718 neither for EBM nor LBM process.

4.1.2 Shrinkage defects

A	Internal defect	I
A2	Shrinkage defects	II
A2.1	Shrinkage defect	At

Definition:

A shrinkage defect is caused by the contraction of the material during the solidification of the melt pool.

Morphology:

Due to the physical phenomenon, all studies described the shrinkage defects as flat voids, close to a crack geometry. No rims or unmelted powder are found in this type of defect.

On one hand, for LBMed alloy Ti6-4, Song et al. [44] showed cracks of hundreds of micrometers length and dozens of micrometers width , rather vertically oriented despite the absence of built direction indication given by the authors in Figure 14.

On other hand, two studies [45], [46] mentioned shrinkage defects for EBMed alloy 718 as illustrated by Figure 15 and Figure 16. Sames (Figure 15) exhibited flat defects under $20\ \mu m$ large and few micrometers thick oriented around 45° compared to the built direction whereas the other study (Figure 16) exhibited shrinkage defects around $100\ \mu m$ large and dozen micrometers thick, oriented rather perpendicular to the built direction. Balachandramurthi et al. [46] showed string patterns of shrinkage defects (Figure 17) perpendicular to the built direction. Each string pattern is distant of around $350\ \mu m$ high. There is no shrinkage defects in the contour region.

Physical origin

Song et al. [44] report the presence of this type of defect in SLMed alloy Ti6-4 for single tracks built at a high energy power and low scanning speed. They attributed these cracks (Figure 14) to a high retraction and residual stress. For EBMed alloy 718, Sames [45] gave the same explanation, he even assumed that could be considered like hot cracking.

In contrast, Balachandramurthi et al. [46] assumed shrinkage defects are caused by a too low energy input linked to the control parameters of the electron beam. For supporting their assumption, they highlighted the space of $350\mu m$ corresponds to five layers. For their builds, the orientation of the hatching theme changes at each layer for 5 consecutive layer. After the 6th layer, the orientation of the melting them is the same than for the first layer. In their opinion, every five layers, the beam parameters are not suitable for the alloy 718 due to the Arcam software that lead to a too low energy input.

Special features for EBM, LBM, Al, Ti or Ni alloy

According to the literature, only SLMed alloy Ti6-4 and EBMed alloy 718 are concerned by shrinkage. Balachandramurthi [46] specify that shrinkage defects are only present in EBMed alloy 718.

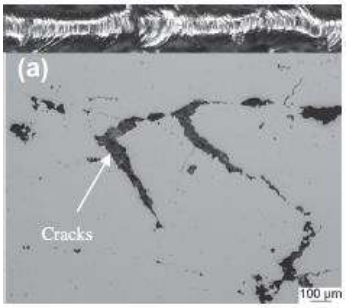

Figure 14: Shrinkage defects reported for SLMed alloy Ti6-4 in a single track from [44], Top – OM of the single track – Bottom – cross-sectional of the single track.

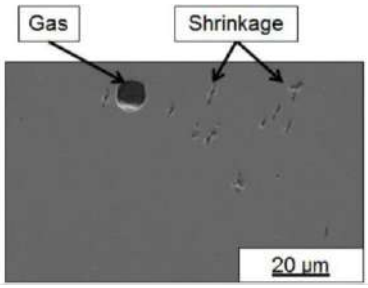

Figure 15 : Skrinkage defect in EBMed alloy 718 from [45].

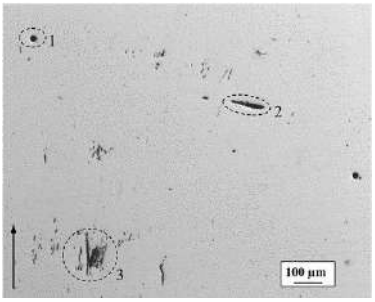

Figure 16 : Defects in EBMed alloy 718 – Number 2 correspond to shrinkage defect from [46].

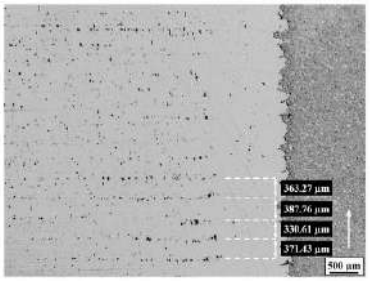

Figure 17 : String pattern shrinkage defects in EBMed alloy 718 from [46].

4.1.3 Lack of fusion defects

In the light of Stef's study [18], these type of defects are created at the interface between melt pools. In practice, the presence of lack of fusion defects is generally due to a combination of phenomenon. It is difficult to isolate in practice only one factor at the origin of the lack of fusion defect.

A	Internal defect	I
A3	Lack of fusion defects	II
A3.1	Hatching induced LOF	III

Definition:

A hatching induced lack of fusion is a lack of fusion occurring between two parallel melt pools belonging to the same layer as illustrated in Figure 19. Gong et al. [32] named this type of defect "Line Offset (LO) Defects".

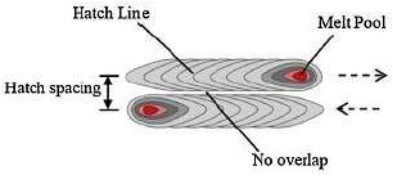

Figure 19 : Illustration of the hatch spacing without overlap from [30].

Morphology

This type of defect are - in theory - pyramid-shaped or trapezoidal as illustrated by Figure 20, if the defect is observed in a slice parallel to the building direction. Unmelted powder is in theory present in the void. This type of voids are located along the hatch lines.

From experimental results, Stef [18] found an equivalent diameter[2] between $5\mu m$ and $20\mu m$ and an aspect ratio[3] between 1.7 and 1.9 for this type of defects in LBMed alloy Ti6-4 as illustrated by the Figure 18.

Mean diameter distribution

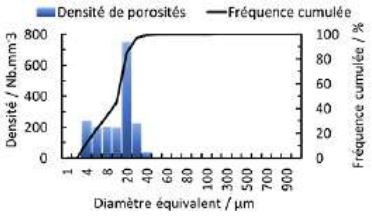

Aspect ratio distribution

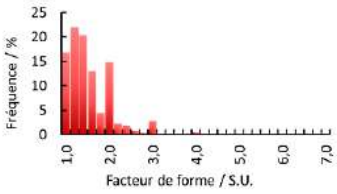

Figure 18 : Mean diameter and aspect ratio distributions of hatching induced LOF for LBMed alloy Ti6-4 from [18].

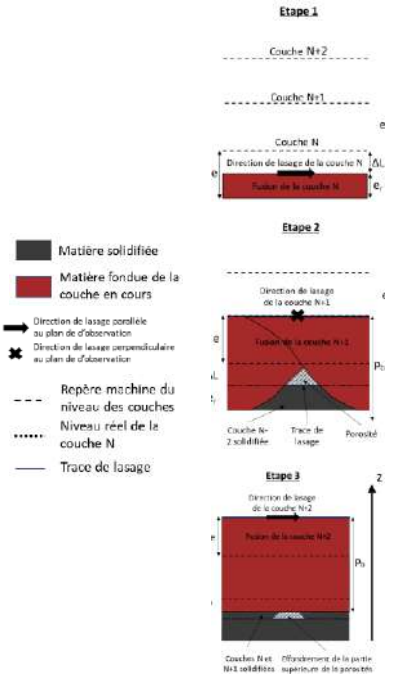

Figure 20: Schema of the metallurgical origin of hatching induced LOF from [18].

Physical origin

The hatching induced lack of fusion is widely studied but most papers assess the global impact of the hatching spacing in term of density of the bulk material. The most detailed studies about this type of defect are presented by Gong et al. and Stef [18], [32].

A too small overlap between two hatch lines or a local lack of powder due to ejection for example [47]–[49] modifies the wetting and the thermal conduction of the melt pool [32]. Then, as shown in Figure 20, , a local surface of the previous layer is not wetted by the melt pool of the new layer because of too important surface tension effect, in other words, because of a contact angle higher than 90° (Figure 21). The void can be filled when the upper layer is melted: if the penetration is significant, the void may partially or totally collapse, if the penetration is low may the void may remain intact.

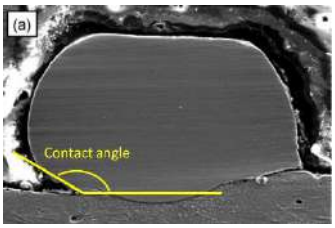

Figure 21: Illustration of the contact angle on stainless steel single scan track made by LBM. Adapted from [50].

Special features for EBM, LBM, Al, Ti or Ni alloy

All processes and alloys are concerned.

[2] Stef [18] defined the equivalent diameter as $D_{eq} = \sqrt[3]{6.V/\pi}$ where V is the volume of the defect detected by mean of RX µCT scan.
[3] Stef [18] defined the aspect ratio as $F = d_{max}/d_{min}$ where d_{max} and d_{min} are the maximum and the minimum length of the defect detected by mean of RX µCT scan also called the *Feret*'s diameter.

A	Internal defect	I
A3	Lack of fusion defects	II
A3.2	Interlayer LOF	III

Definition:

An interlayer lack of fusion is a lack of fusion occurring between two consecutive layers as illustrated in Figure 22. This term is employed by Zhang et al. [51].

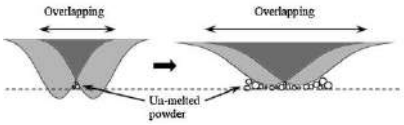

Figure 22: Schema of a interlayer LOF from [30].

Morphology

This type of defect is irregularly shaped, between two layers, and often contains unmelted powder [51]. Hrabe and Quinn [52] confirmed this assumption with optical observations as illustrated by Figure 23 : regardless the distance from the build plate, they observed thin pores, less than $10\ \mu m$ height in the build direction (z) for hundred micrometers length. They added fracture surfaces observation (Figure 24) on which they identified interlayer LOF. The bottom of the interlayer LOF defect (Figure 24(b)) shows a flat surface of $300\ x\ 250\ \mu m^2$ where some rims appear, revealing melting vectors of the melt pool. There are also almost aligned tear marks. The top of the interlayer LOF defect (Figure 24(d)) shows some unmelted powder and partial melted powder. In fact, the fracture initiated on this defect, the powder only sintered made the tear marks on the bottom surface.

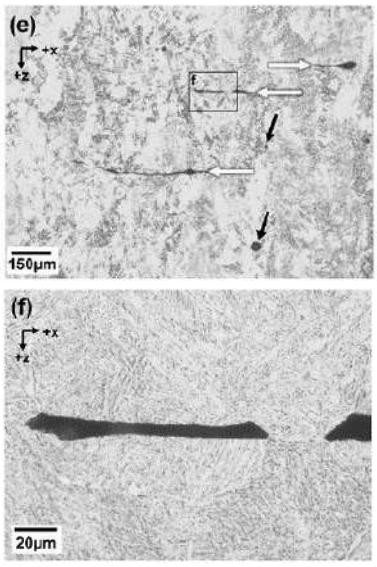

Figure 23 : Micrograph of defect in EBMed alloy Ti6-4 (e) pores – (f) zoom on an interlayer LOF from [52].

Physical origin

An interlayer lack of fusion is generally created by an insufficient energy density provided to create a melt pool through the last powder layer and the already solidified layers [18], [30], [33], [51], [52]. There are several factors which can lead to this type of defects: a too low energy or a too high powder layer thickness. The first factor can be induced by improper parameters, such as beam power and scan speed. The second can induce surface defects on the previous layer. In these cases, at least, there is an irregular penetration or even no penetration of the melted material in the previous layer otherwise there is just a wetting of the powder surrounding the melt pool. These physical origins are quite close from the previous group "Hatching induced LOF", it is sometimes difficult to clearly classify a LOF in one group or another.

The optimization of the beam parameters such as power and scan speed as well as the raking system and the surface roughness of the last melted layer prevent the generation of this type of defects.

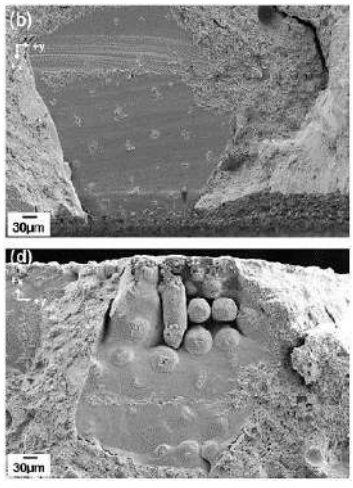

Figure 24 : Interlayer LOF on a fracture surface of EBMed alloy Ti6-4 specimen (b) bottom – (d) top from [52].

Special features for EBM, LBM, Al, Ti or Ni alloy

All processes and alloys are concerned.

4.1.4 Cracks

A	Internal defect	I
A4	Cracks	II
A4.1	Liquation cracking	III

Definition:

Liquation cracking is a crack which occurs in the partial melted zone (PMZ). This zone is defined like the zone where liquid and solid phases are coexisting during the solidification, Figure 25 [53].The PMZ is the interface between the solid material and the melt pool. This crack is intergranular and present an irregular morphology, often following the dendritic morphology.

Morphology

Despite liquation cracking is a well-known phenomenon in welding, and Attallah et al. [54] asserted "other cracking mechanisms such as liquation and solidification cracking, which could occur during welding of alloys, regardless of the chemistry. », there is no liquation crack identified and observed in literature for the couples {process + alloys} addressed in this document.

Physical origin

Due to the lack of reference in powder bed fusion literature, the reader is invited to refer directly to the studies of Kou, Fournier dit Chabert, Carter et al. and Attallah et al. [53]–[56].

Special features for EBM, LBM, Al, Ti or Ni alloy

Liquation cracking is reported for another LBMed Ni based alloy (alloy 738), containing more additional elements than alloy 718 [54], [56]

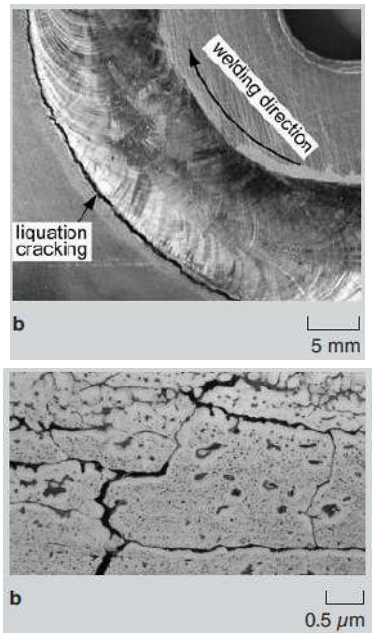

Figure 25: Macrograph (top) and micrograph of a liquation cracking in an aluminum weld from [53].

A	Internal defect	I
A4	Cracks	II
A4.2	Solidification cracking	III

Definition:

Also often called “Hot tearing”, solidification cracking occurs during solidification into the melt pool (Figure 26) [53]. As liquation, solidification is an intergranular crack, but present a morphology more regular, straighter than a liquation crack. The two phenomenon are often tricky to discriminate.

Morphology

As well as for liquation cracking, despite solidification cracking is a well-known phenomenon in welding, and Attallah et al. [54] assert “other cracking mechanisms such as liquation and solidification cracking, which could occur during welding of alloys, regardless of the chemistry. », there is no solidification crack identified and observed in literature for the couples {process + alloys} addressed in this document. .

Physical origin

As previously, due to the lack of reference in powder bed fusion literature, the reader is invited to refer directly to the studies of Kou, Fournier dit Chabert, Carter et al. and Attallah et al. [45], [53]–[56]

Special features for EBM, LBM, Al, Ti or Ni alloy

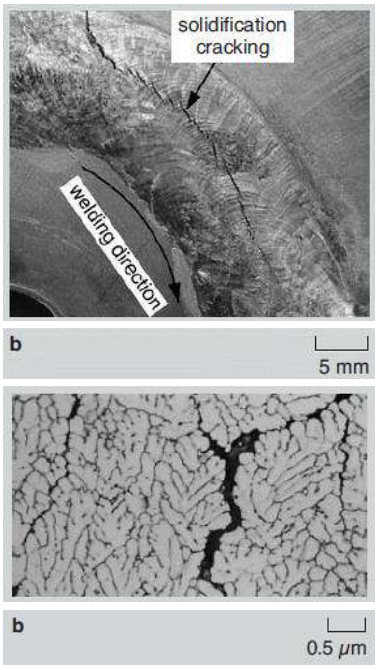

Figure 26: Macrograph (top) and micrograph of a solidification cracking in an aluminum weld from [53].

4.1.5 Undesired phases

A	Internal defect	I
A5	Undesired phases	II
A5.1	Inclusion	III

Definition:

An inclusion on the bulk material is generally created with foreign material that contaminates the powder.

Morphology

By mean of X-rays CT scan analysis (Figure 28), Neikter et al. [57] exhibited inclusion with an approximate diameter of $150\mu m$ in EBMed alloy Ti6-4. The high intensity of the particle on the scan significate that it is composed of dense elements. By mean of optical micrograph (Figure 29), Brandao et al. [58] exhibited inclusion with a diameter below $100\ \mu m$. In these pictures, there is a void between the titanium matrix and the inclusion. By mean of X rays CT scans, a statistically representative population of inclusions was characterized (Figure 50): it appears the inclusions are spherical since the projected area are equivalent in all section plans. Figure 27 shows inclusions on a fracture surface of EBMed alloy Ti6-4 tensile specimen. There are quite spherical with a diameter around $20\ \mu m$.

Physical origin

As highlighted by Neikter et al. and Brandao et al. [57], [58] in their articles, in EBMed alloy Ti6-4, only tungsten inclusions were found. Their investigations led to two assumptions for explaining the phenomenon. The Plasma Rotating Electrode Process (PREP) used to produce Ti6-4 powder could be the first origin of the tungsten contamination as a tungsten electrode is used. This assumption is supported by the shape of the inclusion found by Neikter et al. [57]. The donut shape indicates a void formed during the solidification of the inclusion, probably due to the gas used in the PREP.

Brandao et al. [58] assume the inclusion comes from a cross contamination due to a previous batch of tungsten specimens manufactured with the machine.

These inclusions are hard and brittle. Due to the melting point of the tungsten twice as high as the titanium (3422°C vs 1668°C), these inclusions are not melted during the AM process.

Special features for EBM, LBM, Al, Ti or Ni alloy

In the EBMed alloy 718 specimens no high density inclusion was found [57]. There is no mention of inclusion for SLMed alloy AS7G06. Improper cleaning of the machine can also lead to this type of pollution.

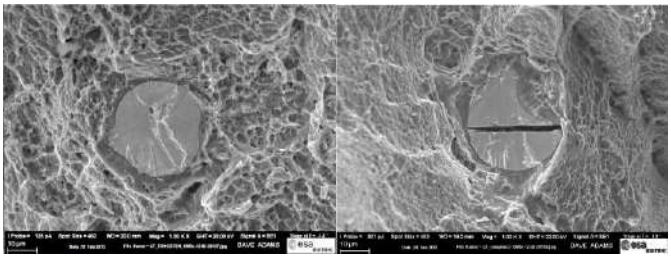

Figure 27 : Fractography of tensile specimens (LBMed alloy Ti6-4) showing inclusions from [58].

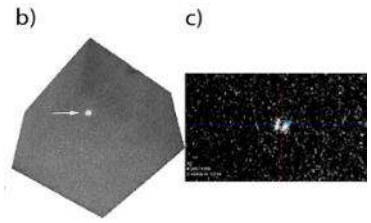

Figure 28: RX CT scan of an EBMed alloy Ti6-4 sample, successive magnifications (b & c) on an inclusion of $150\ \mu m$ approximate diameter from [57] – No scale indicated by the authors on the picture.

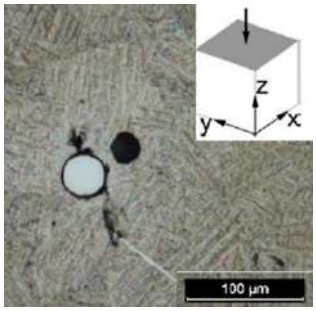

(a)

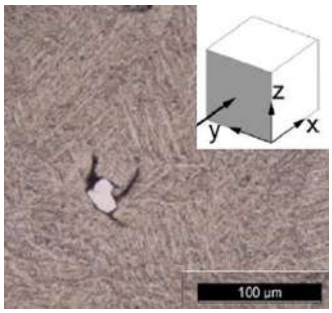

(b)

Figure 29: Micrography of LBMed alloy Ti6-4 showing inclusion (a) X-Y section – (b) Y-Z section modified from [58].

A	Internal defect	I
A5	Undesired phases	II
A5.2	Precipitates	III

Definition:

A precipitate is a dispersed phase formed into a main phase, a matrix.

In some cases, for structural strengthening for example, this phase is voluntarily formed by heat treatment to enhance the material behavior. Precipitates formation after heat treatment or ageing are exposed in the following ANDURRO projects deliverables LIV-M-031-L6-480-v0 and LIV-M031-L6-491 [59], [60]

In the following paragraph, only precipitates formed in as built condition and potentially considered as undesirables will be presented.

Morphology

Thijs et al. [61] highlighted the presence of Ti_3Al precipitates in the vicinity of the melt pool for LBMed alloy Ti6-4. They noted concentration of these intermetallic precipitates around the melt pool by mean of EDX analysis as illustrated by Figure 30: they interpreted the local increase of Al content as presence of Ti_3Al precipitates. There is no specific analysis of these precipitate such as micrograph presented in this study.

There are many precipitates in alloy 718 which is a precipitate-strengthened alloy. Polonsky et al. and Sun et al. [62], [63] highlighted carbides and nitrides precipitates in SLMed (Figure 31) and EBMed alloy 718. These precipitates are very small, below the micron. Sun et al. showed these precipitates are aligned along the build direction.

Physical origin

The formation of the Ti_3Al precipitates is explained by the increase of Al content in local area. As the solubility of the Al in the Ti is low around $550°C$, Ti_3Al precipitates. The precipitation is enhanced by the decreasing of the scan speed or of the hatch spacing. According to several studies, this phase decrease the ductility of the Ti6-4 alloy [64]–[66].

The carbides and nitrides shown by Polonsky et al. and Sun et al. [62], [63] are formed due to the high cooling speed. Al, Ti and Nb segregate in the liquid thus promoting the formation of intermetallic particles such as TiN and NbC. Sun et al. precised the build height is a key parameter for the formation of these precipitates.

Special features for EBM, LBM, Al, Ti or Ni alloy

No significant study was found about the impact of undesirables precipitates in AMed aluminum alloys as built.

In conventionally processed alloy 718, Laves phases are considered as detrimental precipitates since they are brittle. In AMed alloy 718, Laves phases are around 10 times smaller and so less detrimental than in conventional process: no study was found about their detrimental effect. Hugues [67] detailed the formation of the Laves phases in ANDURRO project deliverable LIV-M-031-L6-409-v0.

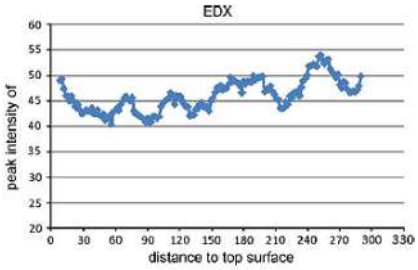

Figure 30 : Depiction of Al content by mean of EDX analysis along a vertical line from the top to the bottom in a LBMed alloy Ti6-4 specimen from [61].

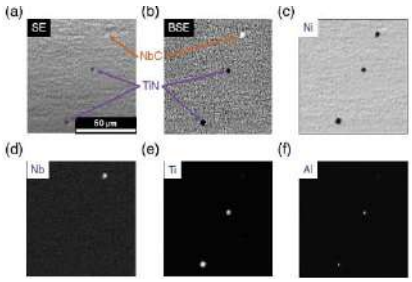

Figure 31: Carbide and nitride precipitates in SLMed alloy 718 from [62].

A	Internal defect	I
A5	Undesired phases	II
A5.3	Oxides	III

Definition:

An oxide is formed by an anion, generally oxygen and a metallic cation. Sometimes, oxide is considered as inclusion [3]. In case of AM, the oxide can form thin films, and is considered as a particular undesired phase.

Morphology

The literature does not report case of detection of the oxides by NDT. All oxides are detected on fracture surfaces or on micrographs, with the help of EDX analysis.

For LBMed and EBMed alloy 718, [62], [68] reported the presence of inclusions in the material. Liu et al. show fracture surface without showing the associate EDS analysis, but from the size of the dimples, these inclusions have a diameter in the micron order. Polonsky showed micrographs (Figure 32) where a micrometric oxide inclusion of Al_2O_3 is entrapped in a TiN or NbC precipitate.

Irregular shaped voids surrounded of a thick oxide film, as illustrated in Figure 33, are mainly reported [69]–[71] for LBMed aluminum alloy. These oxide films cover an area of several hundred of μm^2. Tang and Pistorius showed another shape of oxide defect: sub-micron particles. They proposed an assumption for the formation of the two types of oxide defects as explained later.

Tradowsky et al. [70] showed oxide layer and the potential voids or cracks associate do not disappear after HIP treatment as showed in Figure 34.

Physical origin

All studies [54], [62], [68]–[72] converge on the two same assumptions for explaining the formation of oxide layer or oxide inclusion: a contamination of the powder during its production or its storage or a too high oxygen concentration in the building chamber due to a poor quality of the shielding gas or to a low vacuum function of the process (LBM or EBM).

For alloy 718, a low oxygen content may directly form oxide inclusions such as Al_2O_3, TiO_2, and ZrO_2 [62] . Theses inclusions are then germination sites for precipitates such as nitrides or carbides.

Aluminum alloys are more favorable to the formation of oxide layer covering the last melted layer or surrounding the powder than to the formation of inclusions. As illustrated by Figure 35, the oxide layer on the last layer decreases the wetting of the substrate and this oxide layer (Al_2O_3) requires more power to be melted. Thus the probability to form an interlayer LOF, with unmelted powder entrapped in the void, increases. The oxide layer can also be broken by the melt pool without being melted and entrapped in the material. The same mechanism applied to the oxide layer surrounded the powder is described by Tang and Pistorius [71] to explain sub-micron oxide found in the material.

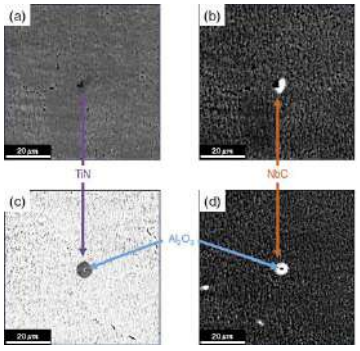

Figure 32: SEM micrograph of oxide inclusions entrapped in a nitride (c) or a carbide in EBMed alloy 718 from [62].

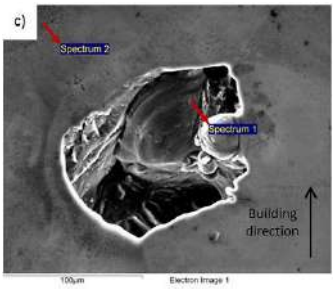

Spectrum	O	Mg	Al	Si	Total wt. %
1	19.44	0.66	70.13	9.77	100
2	3.38	0.53	86.78	9.30	100

Figure 33 : Void surrounded by oxide layer in LBMed alloy AlSi10Mg from [70]

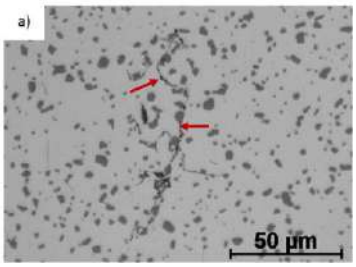

Figure 34 : Micrograph of LBMed alloy AlSi10Mg after T6 and HIP treatment showing a crack induced by oxide layer (red arrows) from [70].

Special features for EBM, LBM, Al, Ti or Ni alloy Despite the high oxidation sensitivity of titanium alloys, no oxide-linked defect was reported for AMed titanium alloy in as built condition for this literature review.	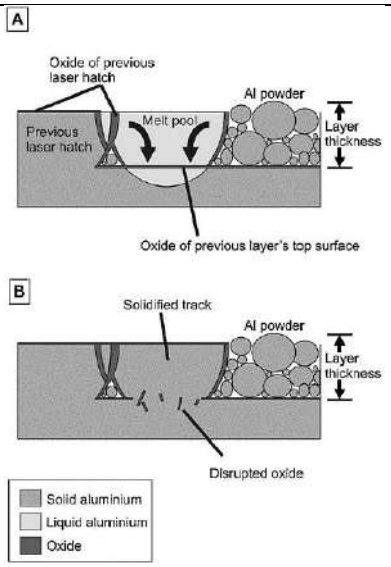 *Figure 35: Mechanism of the oxide entrapment for LBMed aluminum alloy from [72].*

A	Internal defect	I
A5	Undesired phases	II
A5.3	Microstructural heterogeneity	III

Definition: Microstructural heterogeneity is gradient in the alloy microstructure such as local grain size changes, local morphological grain changes, gradient of crystallographic texture or changes of the repartition of different phases in the material. Morphology Microstructural gradients are well known in AM, and have been developed for the three alloys and the associate processes in ANDURRO project deliverables LIV-M-031-L01-049 and LIV-M-031-L1-435-V0 [67], [73].	

4.2 Surface defects

B	Surface defect	I
B1	Melt pool induced	II
B1.1	Balling	III

Definition:

The balling is define as a discontinuity of the melt pool track as illustrated by the single tracks at a low laser power on the left of the Figure 36.

Morphology

As balling is strongly linked to the geometry of the melt pool, this type of defect have the same order of magnitude than the melt pool. Except on the last melted layer, this defect is not visible. But the irregularity formed (Figure 37) on the melted surface due to the balling leads to irregular layer thickness. As seen previously, irregular layer thickness lead to interlayer LOF.

Physical origin

The balling is linked with the surface tension of the melt pool and the wettability of the substrate. Balling occurs when a critical geometry of the melt pool is reached: Yadroitsev [74] identify a critical geometry for laser melted stainless steel: if the length to width ratio of the melt pool is superior to π, $L/W > \pi$ balling occurred.

Most of the studies dealing with defects in AM mention balling [7]–[9], [75], [76].

Promoppatum et al. [77] build a process map for LBMed alloy Ti6-4: balling effect occurred at a combined high scan speed and high laser power.

Special features for EBM, LBM, Al, Ti or Ni alloy

All processes and alloys are affected.

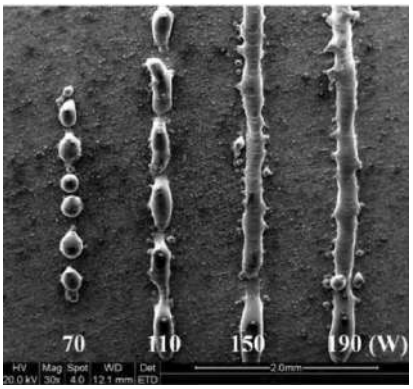

Figure 36 : SEM images of balling phenomenon of LBMed stainless steel single tracks from [8].

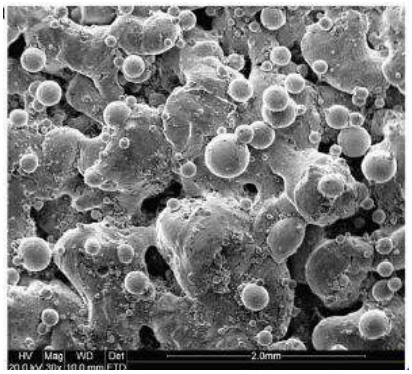

Figure 37: SEM observation showing the irregular morphology of a surface submitted to extreme balling [7].

B	Surface defect	I
B1	Melt pool induced	II
B1.2	Spattering	III

Definition:

The spattering is the ejection of melted material on the solidified material or on the powder as illustrated on Figure 38 [78].

Morphology

References found in the literature dealing with the spattering phenomenon are associated to LBM and stainless steel [78] or Invar36 [49], [79]. These two teams show spatter particles of hundreds of micrometer of diameter as illustrated by Figure 39 and Figure 40. This diameter should be compared with the powder size and the layer thickness: $22 - 70\mu m$ for the LBMed stainless steel and $5 - 70\mu m$ for the LBMed Invar36.

Physical origin

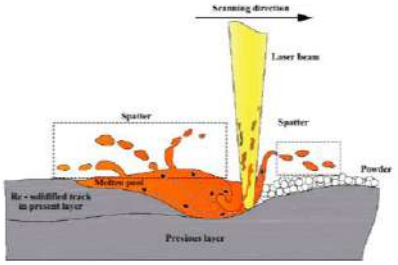

Figure 38: Schema of the spattering phenomenon during laser melting (D. Wang, Dou, and Yang 2018)

Spatter particles come from an ejection of the molten material due to the violent heating caused by the laser beam [80]. Depending on the initial state of the particle, totally or partially melted, its trajectory and the material on which it lands, the spatter could, in the worst case, being sintered on the last melted layer as illustrated on Figure 41. If the spatter particle is not removed by the recoater and larger than the powder, it can be partially melted or not melted. Thus, the spatter particle is entrapped in the bulk material. Spattering often appears simultaneously with keyhole. Assuncao et al. [25] suggested to favor conduction mode for avoiding spattering.

Spatter particles have to be kept in mind during fracture surface analysis: if the void is around hundreds of micrometers of diameter, it may be due to a spatter particle and not to entrapped gas.

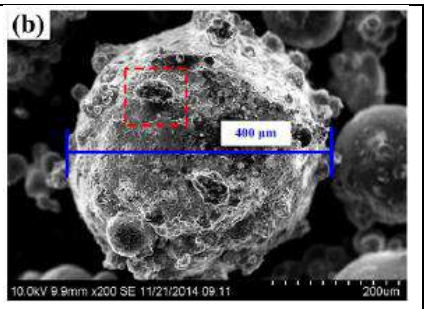

Figure 39 : SEM observation of a spatter particle induced by LBMed stainless steel [78].

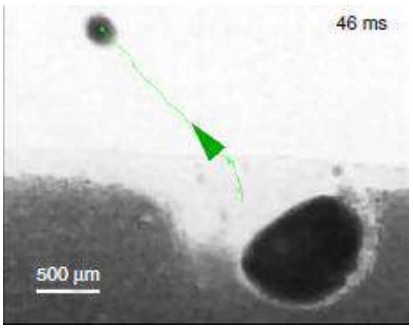

Figure 40 : Ejection of a spatter particle caught by mean of X-ray synchrotron [49].

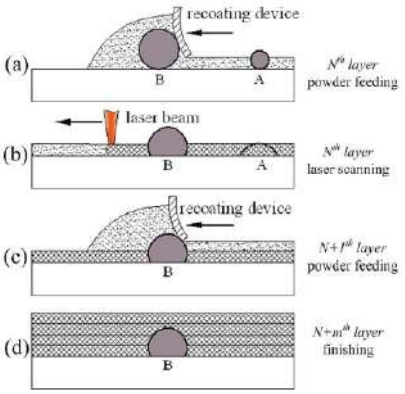

Figure 41: Schema of the consequence of the spatter particle deposited on the last layer from [78].

Special features for EBM, LBM, Al, Ti or Ni alloy

There is no reference dealing with spattering associated to the couple of {process/alloy} studied in the ANDURRO project.

Nevertheless, there is no clear reason not to extrapolate the previous results to our couple {process/alloy}.

B	Surface defect	I
B1	Melt pool induced	II
B1.3	Swelling	III

Definition:

Swelling is a little wave above the plane of melting [45]. This phenomenon is quite similar to humping in framework of welding.

Morphology

Swelling are little waves at the top of the parts. The surface present regular patterns (Figure 42).

Physical origin

The swelling is due to surface tension effects function to the melt pool geometry [45]. Sames attributed the origin of the swelling to a parameter called “turning point” for EBM. The optimization of this parameter allow the disappearance of the swelling (Figure 43). He compared the swelling to the humping for welding.

Special features for EBM, LBM, Al, Ti or Ni alloy

No swelling was reported in another case than EBMed alloy 718.

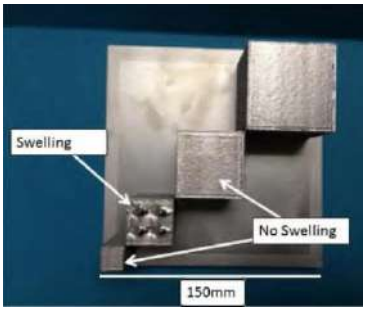

Figure 42: Parts showing swelling and no swelling for the same process parameters for EBMed alloy 718 from [11].

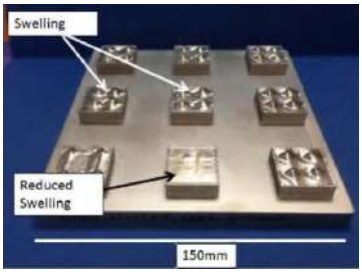

Figure 43: Optimization of process parameters for swelling reducing in EBMed alloy 718 parts from [11].

B	Surface defect	I
B2	Cracks	II
B2.1	Residual stresses induced	III

Definition:

Residual stresses are defined in the literature as the stresses remaining in a part in absence of external loading such as mechanical loading or thermal loading [54] . Residual stress gradient, optically invisible, may induce visible defects such as warpage, global or local part deformations, delamination or cracks (Figure 44).

Despite residual stresses have well known consequences on the mechanical properties, only these visible consequences of the residual stress will be described hereafter, and more specifically the induced defects such as cracks and delamination that fall into the category of “A- internal defects” according to our classification. Authors described sometimes these defects as thermal cracks [81].

Morphology

Residual stresses are closely linked to the geometry of the fabricated part. Thus, the morphology (size and shape) of the induced cracks and delamination will be linked with the geometry. Figure 45 and Figure 46 illustrate the type of cracks induced by residual stresses. On Figure 45, the crack may be considered as delamination crack since it seems to be perpendicular to the building direction. The Figure 46 shows a crack of few millimeters length on the top of a SLMed bridge. On the top of the bridge

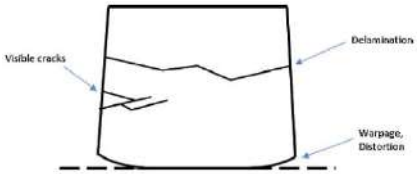

Figure 44 : Cracks and distortion defects, consequence of the residual stresses from [87].

the crack seem to follow the roughness whereas on the front of the bridge, the crack is more or less inclined.

Physical origin

The origin and the complexity of the residual stress is widely discussed in the literature [82], [45], [54], [83]–[85].

Asserin [82] summarize the three phenomenon which lead to the residual stresses:

- Temperature gradient associate to the clamping of the parts;
- The metallurgical transformations which lead to volume change;
- Difference of thermal expansion coefficient (between the build plate and the part mainly).

Mercelis et al. [86] provide a concise explanation of the first phenomenon leading to "global" residual stresses which is illustrated in Figure 47. By considering only the irradiated zone, they explained residual stresses result to differential and localized thermal gradients induced by the melt pool.

About the second phenomenon, the thermal contraction of the melted material during its solidification combined to the constraint of the underlying solidified material induce a stress gradient. The top layer is rather submitted to tensile stress whereas the underlying layer is submitted to compressive stress.

If the residual stresses exceed the yield strength, critical defects such as permanent distortion, warping or even cracks may appeared in the part [54], [87].

The main influencing parameters on residual stresses apparition are the shape of the part, in particular the slenderness ratio, and the scanning strategy [85], [86]. Both parameters affect thermal gradient in the part. Kruth et al. [81] present an interesting mean of residual stress assessment function of the scanning strategy: they built bridge with several scanning strategies and they measure the curling angle after removing the bridge from the base plate (Figure 48). By comparing the curling angle α of the bridges, they assessed the scanning strategy which induced the less residual stress.

A non-intuitive idea is highlighted in these studies: residual stresses intensity is inversely proportional to the pores density. Indeed, as pores have free surfaces, residual stressed may be relaxed by pores deformation. Therefore, caution should be exercised when parameters are optimized to reduce porosity in manufactured parts. This can lead to the creation of significant residual stresses. Compromises between a decrease of the porosity and increase of the residual stresses may be necessary to achieve a targeted part quality.

Special features for EBM, LBM, Al, Ti or Ni alloy

In the literature, studies [88]–[90],compiled by Hugues et al. [67], assessed the maximal value of residual stress between around $100MPa$ and $775MPa$ in LBMed alloy Ti64 parts.

In contrary, studies show that EBM process is almost not concerned about residual stresses. Two research groups measured residual stresses by mean of neutron diffraction experiments. By comparing residual stresses in alloy 718 specimens made by Direct Laser Metal Deposition and EBM, Sochalski-Kolbus et al. [91] showed residual stresses are negligible in EBMed alloy 718 specimens. Hrabe et al. [92] measured no significant residual stress, and thus concluded to the absence of residual stress in EBMed alloy Ti6-4 specimens.

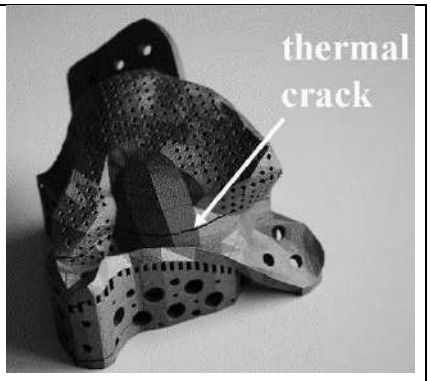

Figure 45: Residual stresses induced crack in LBMed part from [81].

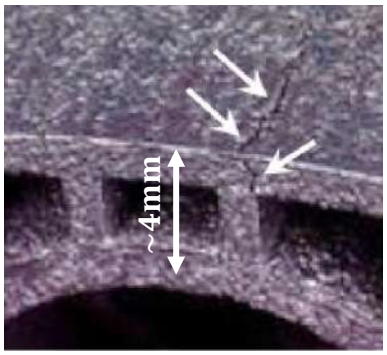

Figure 46 : Illustration of a crack at the top of a SLMed bridge from [93].

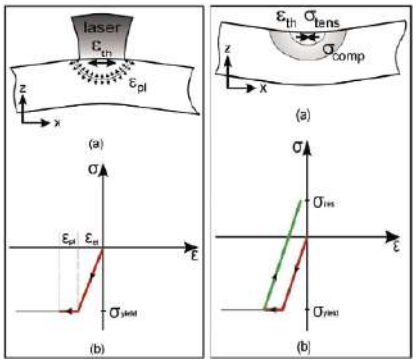

Figure 47 : Thermal Gradient Mechanism (TGM) leading to the residual stress in a single melt pool from [81].

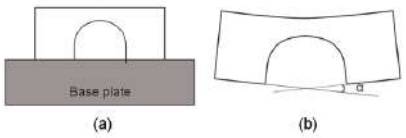

Figure 48: Bridge curling measurement for residual stress assessment of LBM process from [81].

5 Outlook

The classification presented above aims to be the structure of the defect database.

Considering the huge amount of specimens which will be manufactured, tested and analyzed, it seems to be important to capitalize as much information as possible from these specimens especially since a significant number of defect analysis is planned in the framework of the ANDDURO project. In particular, a large amount of micrographs, RX CT scans and fractographs will allow to precise the distribution and the morphological features of each class of defects.

This type of information is quite rare in the literature. Three studies are particularly noteworthy for proposing both a classification: Gong, Brandao et al. and Stef [18], [58], [94]. The results of their works are presented in Figure 49 and Figure 50.

Critère	Distribution de tailles	distribution de facteurs de forme	Dmoyen	Fmoyen
Manque de fusion	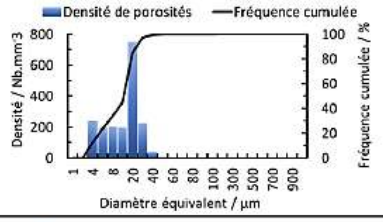	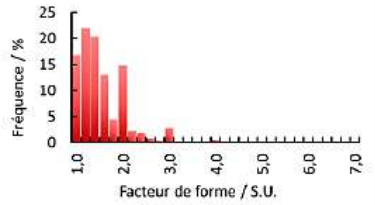	/	1,7 - 1,9
Dénudation	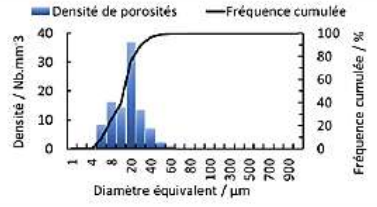	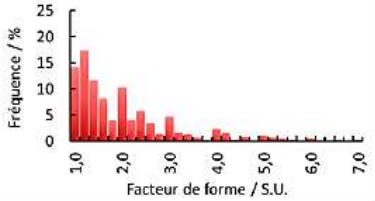	/	2,2 - 2,4
Ejection de matière	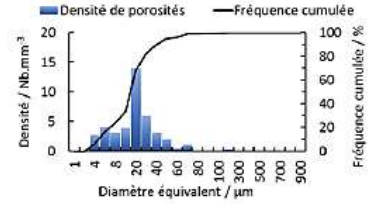	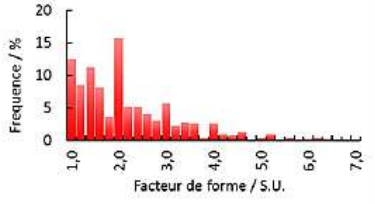	/	2,2 - 2,4
Keyhole	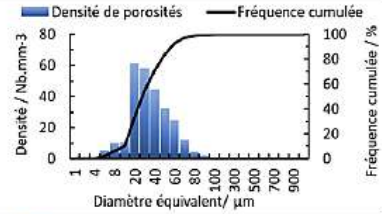	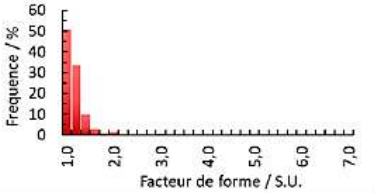	25 µm - 35 µm	1,3 - 1,4
Gaz	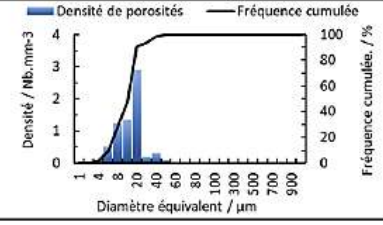	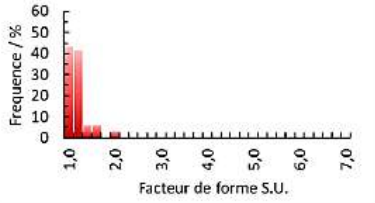	10 µm - 15 µm	1,3 - 1,4

Figure 49 : Classification, size distribution, aspect ratio distribution, mean size and mean aspect ratio of defects analysed in LBMed alloy Ti6-4 from [18].

One point particularly caught our attention in the methodology of Stef's work [18]: for supporting its fracture surface analysis, he superimposed a virtual grid parallel to the fusion path. This method is very helpful for discriminated the defect type.

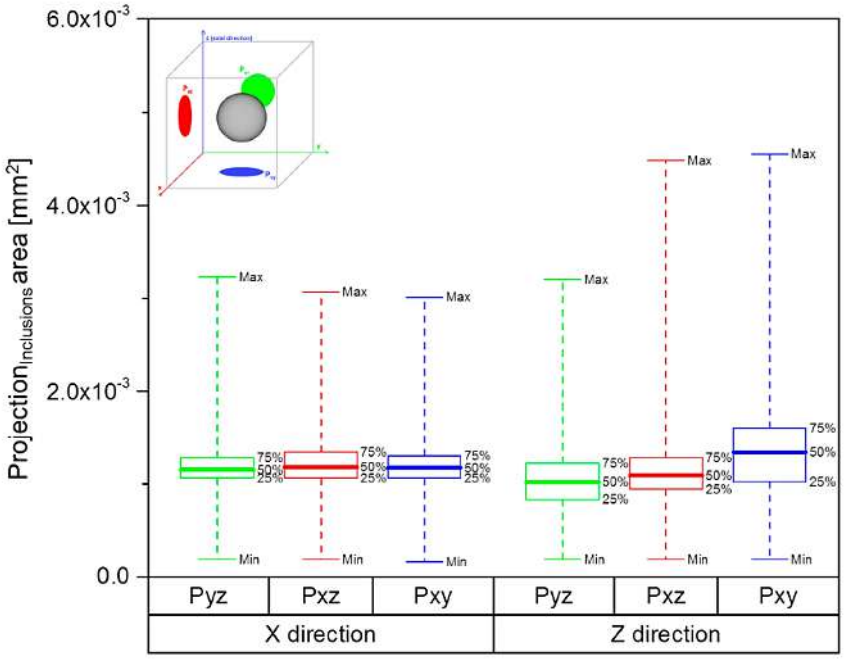

Build Direction	No. Total	Plane	Total Area	Minimum	1st Quartile	Median	3rd Quartile	Maximum
X	153	P_{yz}	1.78×10^{-1}	1.90×10^{-4}	1.06×10^{-3}	1.15×10^{-3}	1.28×10^{-3}	3.23×10^{-3}
		P_{xz}	1.83×10^{-1}	1.90×10^{-4}	1.06×10^{-3}	1.18×10^{-3}	1.34×10^{-3}	3.07×10^{-3}
		P_{xy}	$\mathbf{1.85 \times 10^{-1}}$	1.60×10^{-4}	$\mathbf{1.06 \times 10^{-3}}$	$\mathbf{1.17 \times 10^{-3}}$	$\mathbf{1.30 \times 10^{-3}}$	$\mathbf{3.01 \times 10^{-3}}$
Z	210	P_{yz}	2.23×10^{-1}	1.90×10^{-4}	8.3×10^{-4}	1.02×10^{-3}	1.22×10^{-3}	3.20×10^{-3}
		P_{xz}	2.43×10^{-1}	1.90×10^{-4}	9.4×10^{-4}	1.09×10^{-3}	1.28×10^{-3}	4.48×10^{-3}
		P_{xy}	$\mathbf{2.92 \times 10^{-1}}$	1.90×10^{-4}	$\mathbf{1.02 \times 10^{-3}}$	$\mathbf{1.34 \times 10^{-3}}$	$\mathbf{1.60 \times 10^{-3}}$	$\mathbf{4.55 \times 10^{-3}}$

Figure 50 : Distribution of the projected area of inclusion in LBMed alloy Ti6-4 from (Brandão et al. 2017).

This type of work implies having enough data to lead a statistical approach on specimens to represent the material, which seems possible in the ANDURRO project. This work is tedious but will allow a good evaluation of acceptable and detectable defects for each alloy process pair studied.

6 Conclusions

Based on the work of Fiorese and Bonolo et al. [2], [3], this document proposes both a literature review and a classification for defects found in powder bed fusion for alloys AS7G06, Ti6-4 and 718.

The classification allows, by using data from the literature, to present a morphology description of the defects as well as a physical origin of the defect. The references attached to the physical origin provide sometimes methodological element for studying associated key parameters.

It was shown that some defects such as lack of fusion or keyhole induced pores are closely linked with the process parameters and may be avoided by the optimization of these process parameters. Some defects such as gas entrapment, hydrogen related pores or residual stresses are trickier to mitigate. However, on one hand, the size of the gas related pores are often below above $50\mu m$ of equivalent diameter. It is assumed this size of defects are not very detrimental for the material, even if there is an important cluster of the gas related pores. The work of the WP4 should give some objective element for supporting – or not – this assumption. In other hand, for the residual stresses, if there is no crack created by the stress gradient, a heat treatment may decrease efficiently these residual stresses.

If the proposed classification of the internal defects is quasi exhaustive, there is missing classes for internal defects. For efficiency reasons, we did not consider surface defects which have no impact on the bulk material. All surface defects considered in this document are defects that can cause subsequent internal defects. In the framework of the ANDDURO project, this lack has a negligible impact since all of the analysis are made on machined specimens. The surface roughness is not a parameter in our powder bed fusion assessment.

This proposed classification is the starting point for the defect database implementation in the dedicated IRT's software.

As mentioned in the outlooks, the next step consist to fill this defects database with the project's results.

7 References

[1] H. Gruber, “Electron Beam melting of alloy 718 - Powder recycling and its effect on defect formation,” Licenciate thesis, Chalmers university of Technology, Göteborg, Sweden, 2019.

[2] F. Bonollo, G. Timelli, E. Fiorese, E. Gariboldi, P. Parona, and L. Arnberg, “Database on defect - StaCast Project,” University of Padova - DTG, Italie, D2.1, Mar. 2013.

[3] E. Fiorese, F. Bonollo, G. Timelli, L. Arnberg, and E. Gariboldi, “New Classification of Defects and Imperfections for Aluminum Alloy Castings,” *Int. J. Met.*, vol. 9, no. 1, pp. 55–66, Jan. 2015.

[4] D. Cocks, “A proposed simple qualitative classification for die-casting defects,” in *Proc. Die-casting Conference, Montreaux*, 1996, p. 19.

[5] W. G. Walkington, *Die casting defects: causes and solutions*. North American Die Casting Association, 1997.

[6] J. Campbell, *Castings*. Elsevier, 2003.

[7] D. Gu and Y. Shen, “Balling phenomena in direct laser sintering of stainless steel powder: Metallurgical mechanisms and control methods,” *Mater. Des.*, vol. 30, no. 8, pp. 2903–2910, Sep. 2009.

[8] R. Li, J. Liu, Y. Shi, L. Wang, and W. Jiang, “Balling behavior of stainless steel and nickel powder during selective laser melting process,” *Int. J. Adv. Manuf. Technol.*, vol. 59, no. 9–12, pp. 1025–1035, Apr. 2012.

[9] E. Todorov, R. Spencer, S. Gleeson, M. Jamshidinia, and S. M. Kelly, “America Makes: National Additive Manufacturing Innovation Institute (NAMII) Project 1: Nondestructive Evaluation (NDE) of Complex Metallic Additive Manufactured (AM) Structures,” Air Force materials laboratory, Fort Belvoir, VA, AFRL-RX-WP-TR-2014-0162, Jun. 2014.

[10] AIRBUS, “AIMS 03-22-000 - Airbus Material Specification - Additive Manufacturing Metallic Powder Bed Fusion Technology Titanium Blank Product - Technical Specification.” AIRBUS, Oct-2017.

[11] W. J. Sames, F. Medina, W. H. Peter, S. S. Babu, and R. R. Dehoff, “Effect of Process Control and Powder Quality on Inconel 718 Produced Using Electron Beam Melting,” in *8th International Symposium on Superalloy 718 and Derivatives*, E. Ott, A. Banik, J. Andersson, I. Dempster, T. Gabb, J. Groh, K. Heck, R. Helmink, X. Liu, and A. Wusatowska-Sarnek, Eds. Hoboken, NJ, USA: John Wiley & Sons, Inc., 2014, pp. 409–423.

[12] R. Cunningham *et al.*, “Analyzing the effects of powder and post-processing on porosity and properties of electron beam melted Ti-6Al-4V,” *Mater. Res. Lett.*, vol. 5, no. 7, pp. 516–525, Nov. 2017.

[13] H. Rao, S. Giet, K. Yang, X. Wu, and C. H. J. Davies, “The influence of processing parameters on aluminium alloy A357 manufactured by Selective Laser Melting,” *Mater. Des.*, vol. 109, pp. 334–346, Nov. 2016.

[14] S. Tammas-Williams, P. J. Withers, I. Todd, and P. B. Prangnell, “Porosity regrowth during heat treatment of hot isostatically pressed additively manufactured titanium components,” *Scr. Mater.*, vol. 122, pp. 72–76, Sep. 2016.

[15] X. Zhao, J. Chen, X. Lin, and W. Huang, “Study on microstructure and mechanical properties of laser rapid forming Inconel 718,” *Mater. Sci. Eng. A*, vol. 478, no. 1, pp. 119–124, Apr. 2008.

[16] M. N. Ahsan, A. J. Pinkerton, R. J. Moat, and J. Shackleton, “A comparative study of laser direct metal deposition characteristics using gas and plasma-atomized Ti–6Al–4V powders,” *Mater. Sci. Eng. A*, vol. 528, no. 25, pp. 7648–7657, Sep. 2011.

[17] S. M. Gaytan, L. E. Murr, F. Medina, E. Martinez, M. I. Lopez, and R. B. Wicker, “Advanced metal powder based manufacturing of complex components by electron beam melting,” *Mater. Technol.*, vol. 24, no. 3, pp. 180–190, Sep. 2009.

[18] J. Stef, “Fusion laser sélective de poudre de Ti-6Al-4V : Microstructure et mécanisme de formation des porosités en lien avec les paramètres du procédé SLM et les propriétés microstructurales,” Thèse de doctorat, Université de Bordeaux, Bordeaux, 2018.

[19] G. Kasperovich, J. Haubrich, J. Gussone, and G. Requena, “Correlation between porosity and processing parameters in TiAl6V4 produced by selective laser melting,” *Mater. Des.*, no. 105, pp. 160–170, Jun. 2016.

[20] A. A. Martin *et al.*, “Dynamics of pore formation during laser powder bed fusion additive manufacturing,” *Nat. Commun.*, vol. 10, no. 1, p. 1987, Apr. 2019.

[21] L. Huang, X. Hua, D. Wu, and F. Li, “Numerical study of keyhole instability and porosity formation mechanism in laser welding of aluminum alloy and steel,” *J. Mater. Process. Technol.*, vol. 252, pp. 421–431, Feb. 2018.

[22] C. Teng *et al.*, “A review of defect modeling in laser material processing,” *Addit. Manuf.*, vol. 14, pp. 137–147, Mar. 2017.

[23] T. DebRoy and S. A. David, “Physical processes in fusion welding,” *Rev. Mod. Phys.*, vol. 67, no. 1, pp. 85–112, Jan. 1995.

[24] R. Rai, J. W. Elmer, T. A. Palmer, and T. DebRoy, “Heat transfer and fluid flow during keyhole mode laser welding of tantalum, Ti–6Al–4V, 304L stainless steel and vanadium,” *J. Phys. Appl. Phys.*, vol. 40, no. 18, pp. 5753–5766, Aug. 2007.

[25] E. Assuncao, S. Williams, and D. Yapp, “Interaction time and beam diameter effects on the conduction mode limit,” *Opt. Lasers Eng.*, vol. 50, no. 6, pp. 823–828, Jun. 2012.

[26] W. A. Ayoola, W. J. Suder, and S. W. Williams, “Parameters controlling weld bead profile in conduction laser welding,” *J. Mater. Process. Technol.*, vol. 249, pp. 522–530, Nov. 2017.

[27] W. E. King *et al.*, “Observation of keyhole-mode laser melting in laser powder-bed fusion additive manufacturing,” *J. Mater. Process. Technol.*, vol. 214, no. 12, pp. 2915–2925, Dec. 2014.

[28] R. Cunningham *et al.*, “Keyhole threshold and morphology in laser melting revealed by ultrahigh-speed x-ray imaging,” *Science*, vol. 363, no. 6429, pp. 849–852, Feb. 2019.

[29] H. Zhao and T. DebRoy, “Macroporosity free aluminum alloy weldments through numerical simulation of keyhole mode laser welding,” *J. Appl. Phys.*, vol. 93, no. 12, pp. 10089–10096, Jun. 2003.

[30] H. Gong, K. Rafi, H. Gu, T. Starr, and B. Stucker, “Analysis of defect generation in Ti–6Al–4V parts made using powder bed fusion additive manufacturing processes,” *Addit. Manuf.*, vol. 1–4, pp. 87–98, Oct. 2014.

[31] J. Blackburn, “Understanding porosity formation and prevention when welding Titanium alloys with 1µm laser beams,” Doctor of Engineering, The university of Manchester, Manchester, UK, 2011.

[32] H. Gong *et al.*, “Melt Pool Characterization for Selective Laser Melting of Ti-6 Al-4 V Pre-alloyed Powder,” presented at the 25th, Annual international solid freeform fabrication symposium, Austin, TX, 2014, pp. 256–267.

[33] T. Vilaro, C. Colin, and J. D. Bartout, “As-Fabricated and Heat-Treated Microstructures of the Ti-6Al-4V Alloy Processed by Selective Laser Melting,” *Metall. Mater. Trans. A*, vol. 42, no. 10, pp. 3190–3199, Oct. 2011.

[34] T. Kimura and T. Nakamoto, “Microstructures and mechanical properties of A356 (AlSi7Mg0.3) aluminum alloy fabricated by selective laser melting,” *Mater. Des.*, vol. 89, pp. 1294–1301, Jan. 2016.

[35] A. Aggarwal and A. Kumar, “Particle Scale Modelling of Selective Laser Melting-Based Additive Manufacturing Process Using Open-Source CFD Code OpenFOAM,” *Trans. Indian Inst. Met.*, vol. 71, no. 11, pp. 2813–2817, Nov. 2018.

[36] A. Haboudou, P. Peyre, A. B. Vannes, and G. Peix, “Reduction of porosity content generated during Nd:YAG laser welding of A356 and AA5083 aluminium alloys,” *Mater. Sci. Eng. A*, vol. 363, no. 1, pp. 40–52, Dec. 2003.

[37] R. Xiao and X. Zhang, “Problems and issues in laser beam welding of aluminum–lithium alloys,” *J. Manuf. Process.*, vol. 16, no. 2, pp. 166–175, Apr. 2014.

[38] E. Sallica-Leva, A. L. Jardini, and J. B. Fogagnolo, “Microstructure and mechanical behavior of porous Ti–6Al–4V parts obtained by selective laser melting,” *J. Mech. Behav. Biomed. Mater.*, vol. 26, pp. 98–108, Oct. 2013.

[39] C. Weingarten, D. Buchbinder, N. Pirch, W. Meiners, K. Wissenbach, and R. Poprawe, “Formation and reduction of hydrogen porosity during selective laser melting of AlSi10Mg,” *J. Mater. Process. Technol.*, vol. 221, pp. 112–120, Jul. 2015.

[40] V. I. Lakomski and N. N. Kalinyuk, “The solubility of hydrogen in liquid titanium,” *Autom. Weld.*, vol. 16, pp. 28–32, 1963.

[41] S. Tammas-Williams, H. Zhao, F. Léonard, F. Derguti, I. Todd, and P. B. Prangnell, “XCT analysis of the influence of melt strategies on defect population in Ti–6Al–4V components manufactured by Selective Electron Beam Melting,” *Mater. Charact.*, vol. 102, pp. 47–61, Apr. 2015.

[42] K.-D. Li and E. Chang, “Mechanism of nucleation and growth of hydrogen porosity in solidifying A356 aluminum alloy: an analytical solution,” *Acta Mater.*, vol. 52, no. 1, pp. 219–231, Jan. 2004.

[43] K. V. Yang, P. Rometsch, C. H. J. Davies, A. Huang, and X. Wu, “Effect of heat treatment on the microstructure and anisotropy in mechanical properties of A357 alloy produced by selective laser melting,” *Mater. Des.*, vol. 154, pp. 275–290, Sep. 2018.

[44] B. Song, S. Dong, B. Zhang, H. Liao, and C. Coddet, “Effects of processing parameters on microstructure and mechanical property of selective laser melted Ti6Al4V,” *Mater. Des.*, vol. 35, pp. 120–125, Mar. 2012.

[45] W. Sames, “Additive Manufacturing of Inconel 718 using Electron Beam Melting: Processing, Post-Processing, & Mechanical Properties,” Thesis, 2015.

[46] A. R. Balachandramurthi, J. Moverare, N. Dixit, and R. Pederson, "Influence of defects and as-built surface roughness on fatigue properties of additively manufactured Alloy 718," *Mater. Sci. Eng. A*, vol. 735, pp. 463–474, Sep. 2018.

[47] V. Gunenthiram *et al.*, "Experimental analysis of spatter generation and melt-pool behavior during the powder bed laser beam melting process," *J. Mater. Process. Technol.*, vol. 251, pp. 376–386, Jan. 2018.

[48] N. D. Parab *et al.*, "Ultrafast X-ray imaging of laser–metal additive manufacturing processes," *J. Synchrotron Radiat.*, vol. 25, no. 5, pp. 1467–1477, Sep. 2018.

[49] C. L. A. Leung, S. Marussi, R. C. Atwood, M. Towrie, P. J. Withers, and P. D. Lee, "In situ X-ray imaging of defect and molten pool dynamics in laser additive manufacturing," *Nat. Commun.*, vol. 9, no. 1, p. 1355, Apr. 2018.

[50] R. Li, Y. Shi, Z. Wang, L. Wang, J. Liu, and W. Jiang, "Densification behavior of gas and water atomized 316L stainless steel powder during selective laser melting," *Appl. Surf. Sci.*, vol. 256, no. 13, pp. 4350–4356, Apr. 2010.

[51] B. Zhang, Y. Li, and Q. Bai, "Defect Formation Mechanisms in Selective Laser Melting: A Review," *Chin. J. Mech. Eng.*, vol. 30, no. 3, pp. 515–527, May 2017.

[52] N. Hrabe and T. Quinn, "Effects of processing on microstructure and mechanical properties of a titanium alloy (Ti–6Al–4V) fabricated using electron beam melting (EBM), Part 2: Energy input, orientation, and location," *Mater. Sci. Eng. A*, vol. 573, pp. 271–277, Jun. 2013.

[53] S. Kou, "Solidification and liquation cracking issues in welding," *JOM*, vol. 55, no. 6, pp. 37–42, Jun. 2003.

[54] M. M. Attallah, R. Jennings, X. Wang, and L. N. Carter, "Additive manufacturing of Ni-based superalloys: The outstanding issues," *MRS Bull.*, vol. 41, no. 10, pp. 758–764, Oct. 2016.

[55] F. Fournier dit Chabert, "Rechargement laser d'un superalliage à base de nickel : étude expérimentale et modélisation de l'endommagement," thesis, Nantes, 2007.

[56] L. Carter, M. Attallah, and R. Reed, "Laser Powder Bed Fabrication of Nickel-base Superalloys: Influence of Parameters; Characterisation, Quantification and Mitigation of Cracking," in *Superalloys 2012: 12th International Symposium on Superalloys*, 2012, p. 10.

[57] M. Neikter *et al.*, "Defect characterization of electron beam melted Ti-6Al-4V and Alloy 718 with X-ray microtomography," 2018.

[58] A. D. Brandão *et al.*, "Challenges in Additive Manufacturing of Space Parts: Powder Feedstock Cross-Contamination and Its Impact on End Products," *Materials*, vol. 10, no. 5, p. 522, May 2017.

[59] J. Barot, J.-M. Agullo, J. Hugues, and S. Perusin, "Literature review: influence of heat treatments on aluminium," IRT Saint Exupéry, Toulouse, France, Literature review LIV-M-031-L6-480-v0, Feb. 2019.

[60] B. Max, C. Larignon, and S. Perusin, "Literature review – Alloy 718 elaborated by powder bed fusion technologies: heats treatments," IRT Saint Exupéry, Toulouse, France, Literature review LIV-M031-L6-491, Mar. 2019.

[61] L. Thijs, F. Verhaeghe, T. Craeghs, J. V. Humbeeck, and J.-P. Kruth, "A study of the microstructural evolution during selective laser melting of Ti–6Al–4V," *Acta Mater.*, vol. 58, no. 9, pp. 3303–3312, May 2010.

[62] A. T. Polonsky, M. P. Echlin, W. C. Lenthe, R. R. Dehoff, M. M. Kirka, and T. M. Pollock, "Defects and 3D structural inhomogeneity in electron beam additively manufactured Inconel 718," *Mater. Charact.*, vol. 143, pp. 171–181, Sep. 2018.

[63] S.-H. Sun *et al.*, "Electron beam additive manufacturing of Inconel 718 alloy rods: Impact of build direction on microstructure and high-temperature tensile properties," *Addit. Manuf.*, vol. 23, pp. 457–470, Oct. 2018.

[64] D.-G. Lee and S. Lee, "Effects of nano-sized α2 (Ti3Al) particles on quasi-static and dynamic deformation behavior of Ti-6Al-4V alloy with bimodal microstructure," *J. Mater. Sci.*, vol. 40, no. 15, pp. 4077–4084, Aug. 2005.

[65] L. M. Wang, H. C. Lin, and C. J. Tsai, "Characterization and Mechanism of α2-Ti3Al and γ-TiAl Precipitation in Ti-6Al-4V Alloy Following Tungsten Arc Welding," *Key Eng. Mater.*, vol. 520, pp. 320–329, Aug. 2012.

[66] V. Chastand, "Etude du comportement mécanique et des mécanismes d'endommagement de pièces métalliques réalisées par fabrication additive," PhD Thesis, Ecole Centrale de Lille, Lille, 2016.

[67] J. Hugues, C. Larignon, and S. Perusin, "Literature review – Alloys Ti64 and 718 elaborated by powder bed fusion technologies: microstructure and mechanical properties," IRT Saint Exupéry, Literature review LIV-M-031-L01-049, 2018.

[68] F. Liu *et al.*, "The effect of laser scanning path on microstructures and mechanical properties of laser solid formed nickel-base superalloy Inconel 718," *J. Alloys Compd.*, vol. 509, no. 13, pp. 4505–4509, Mar. 2011.

[69] N. Read, W. Wang, K. Essa, and M. M. Attallah, “Selective laser melting of AlSi10Mg alloy: Process optimisation and mechanical properties development,” *Mater. Des. 1980-2015*, vol. 65, pp. 417–424, Jan. 2015.

[70] U. Tradowsky, J. White, R. M. Ward, N. Read, W. Reimers, and M. M. Attallah, “Selective laser melting of AlSi10Mg: Influence of post-processing on the microstructural and tensile properties development,” *Mater. Des.*, vol. 105, pp. 212–222, Sep. 2016.

[71] M. Tang and P. C. Pistorius, “Oxides, porosity and fatigue performance of AlSi10Mg parts produced by selective laser melting,” *Int. J. Fatigue*, vol. 94, pp. 192–201, Jan. 2017.

[72] E. Louvis, P. Fox, and C. J. Sutcliffe, “Selective laser melting of aluminium components,” *J. Mater. Process. Technol.*, vol. 211, no. 2, pp. 275–284, Feb. 2011.

[73] J. Barot, C. Larignon, and S. Perusin, “Microstructure and mechanical properties of aluminium alloys produced by laser beam melting,” IRT Saint Exupéry, Literature review LIV-M-031-L1-435-V0, May 2018.

[74] I. Yadroitsev, A. Gusarov, I. Yadroitsava, and I. Smurov, “Single track formation in selective laser melting of metal powders,” *J. Mater. Process. Technol.*, vol. 210, no. 12, pp. 1624–1631, Sep. 2010.

[75] N. T. Aboulkhair, N. M. Everitt, I. Ashcroft, and C. Tuck, “Reducing porosity in AlSi10Mg parts processed by selective laser melting,” *Addit. Manuf.*, vol. 1–4, pp. 77–86, Oct. 2014.

[76] H. Taheri, M. R. B. M. Shoaib, L. Koester, T. Bigelow, P. C. Collins, and L. J. Bond, “Powder-based additive manufacturing – a review of types of defects, generation mechanisms, detection, property evaluation and metrology,” *Int. J. Addit. Subtractive Mater. Manuf.*, vol. 1, no. 2, p. 172, 2017.

[77] P. Promoppatum, R. Onler, and S.-C. Yao, “Numerical and experimental investigations of micro and macro characteristics of direct metal laser sintered Ti-6Al-4V products,” *J. Mater. Process. Technol.*, vol. 240, pp. 262–273, Feb. 2017.

[78] Y. Liu, Y. Yang, S. Mai, D. Wang, and C. Song, “Investigation into spatter behavior during selective laser melting of AISI 316L stainless steel powder,” *Mater. Des.*, vol. 87, pp. 797–806, Dec. 2015.

[79] C. L. A. Leung, S. Marussi, M. Towrie, R. C. Atwood, P. J. Withers, and P. D. Lee, “The effect of powder oxidation on defect formation in laser additive manufacturing,” *Acta Mater.*, vol. 166, pp. 294–305, Mar. 2019.

[80] D. Wang, W. Dou, and Y. Yang, “Research on Selective Laser Melting of Ti6Al4V: Surface Morphologies, Optimized Processing Zone, and Ductility Improvement Mechanism,” *Metals*, vol. 8, no. 7, p. 471, Jul. 2018.

[81] J.-P. Kruth, J. Deckers, E. Yasa, and R. Wauthlé, “Assessing and comparing influencing factors of residual stresses in selective laser melting using a novel analysis method,” *Proc. Inst. Mech. Eng. Part B J. Eng. Manuf.*, vol. 226, no. 6, pp. 980–991, Jun. 2012.

[82] O. Asserin, “Quelques enjeux et besoins en modélisation et simulation numérique du soudage,” LaMSID, 26-Nov-2009.

[83] B. Vrancken, “Study of Residual Stresses in Selective Laser Melting,” PhD Thesis, KU Leuven, 2016.

[84] L. Shuai, Q. Wei, Y. Shi, J. Zhang, and L. Wei, “Micro-Crack Formation and Controlling of Inconel625 Parts Fabricated by Selective Laser Melting,” p. 10.

[85] A. E. Patterson, S. L. Messimer, and P. A. Farrington, “Overhanging Features and the SLM/DMLS Residual Stresses Problem: Review and Future Research Need,” *Technologies*, vol. 5, no. 2, p. 15, Jun. 2017.

[86] P. Mercelis and J. Kruth, “Residual stresses in selective laser sintering and selective laser melting,” *Rapid Prototyp. J.*, vol. 12, no. 5, pp. 254–265, Oct. 2006.

[87] J. H. Tan, W. L. E. Wong, and K. W. Dalgarno, “An overview of powder granulometry on feedstock and part performance in the selective laser melting process,” *Addit. Manuf.*, vol. 18, pp. 228–255, Dec. 2017.

[88] S. Leuders *et al.*, “On the mechanical behaviour of titanium alloy TiAl6V4 manufactured by selective laser melting: Fatigue resistance and crack growth performance,” *Int. J. Fatigue*, vol. 48, no. Supplement C, pp. 300–307, Mar. 2013.

[89] M. Simonelli, Y. Y. Tse, and C. Tuck, “Effect of the build orientation on the mechanical properties and fracture modes of SLM Ti–6Al–4V,” *Mater. Sci. Eng. A*, vol. 616, pp. 1–11, Oct. 2014.

[90] P. Edwards and M. Ramulu, “Fatigue performance evaluation of selective laser melted Ti–6Al–4V,” *Mater. Sci. Eng. A*, vol. 598, pp. 327–337, Mar. 2014.

[91] L. M. Sochalski-Kolbus *et al.*, “Comparison of Residual Stresses in Inconel 718 Simple Parts Made by Electron Beam Melting and Direct Laser Metal Sintering,” *Metall. Mater. Trans. A*, vol. 46, no. 3, pp. 1419–1432, Mar. 2015.

[92] N. Hrabe, T. Gnäupel-Herold, and T. Quinn, “Fatigue properties of a titanium alloy (Ti–6Al–4V) fabricated via electron beam melting (EBM): Effects of internal defects and residual stress,” *Int. J. Fatigue*, vol. 94, pp. 202–210, Jan. 2017.

[93] M. F. Zaeh and G. Branner, “Investigations on residual stresses and deformations in selective laser melting,” *Prod. Eng.*, vol. 4, no. 1, pp. 35–45, Feb. 2010.

[94] H. Gong, “Generation and detection of defects in metallic parts fabricated by selective laser melting and electron beam melting and their effects on mechanical properties.,” University of Louisville, Louisville, Kentiucky, 2013.

End of document